Chemosphere 241 (2020) 125133

Contents lists available at ScienceDirect

Chemosphere

journal homepage: www.elsevier.com/locate/chemosphere

Black carbon in Xiamen, China: Temporal variations, transport pathways and impacts of synoptic circulation

Junjun Deng [a, *], Wei Zhao [b], Libin Wu [a], Wei Hu [a], Lujie Ren [a], Xin Wang [a], Pingqing Fu [a]

[a] Institute of Surface-Earth System Science, Tianjin University, Tianjin, 300072, China
[b] State Environmental Protection Key Laboratory of Urban Ecological Environment Simulation and Protection, South China Institute of Environmental Science, MEE, Guangzhou, 510655, China

highlights

- One year on-line observation of BC was conducted in Western Taiwan Strait in China.
- Originations and transport pathways of BC were investigated with CPF, PSCF and CWT.
- Impacts of synoptic circulations on BC from different source sectors were analyzed.

article info

Article history:
Received 20 August 2019
Received in revised form
12 October 2019
Accepted 15 October 2019
Available online 16 October 2019

Handling Editor:

Keywords:
Black carbon
Transport pathway
PSCF
CWT
Synoptic circulation

abstract

Black carbon (BC) plays a vital role in atmospheric environment and climate change. Temporal variations and transport pathways of BC in Xiamen, China with the impacts of synoptic circulation were investigated in 2014 with Aethalometer. Annual mean BC concentration was 4270 ng m^{-3}. BC exhibited clear diurnal (seasonal) variations, with the maximum of 6182 (4755) ng m^{-3} at 6:00 (in spring) and minimum of 2847 (3774) ng m^{-3} at 13:00 (in summer). Conditional probability function analysis indicated that high BC concentrations were associated with northwesterly winds with low wind speed. Air masses originating from the East China Sea and passing along with East China Coast had the highest BC concentrations. Potential source contribution function and concentration weighted trajectory analysis suggested that major sources for BC included the surrounding region, southwestern Fujian and eastern Guangdong to the southwest, Hubei, Hunan and Jiangxi to the northwest, the East China Sea and the South China Sea. Of the nine synoptic circulation patterns, three cyclone-related patterns were associated with low BC concentrations and small biomass burning (BC_{bb}) contributions. Of the six anticyclone-related patterns, the three cold-high circulations around winter were associated with moderate BC concentrations and large BC_{bb} contributions. The two cold-high patterns in spring and autumn were associated with high BC concentrations and small BC_{bb} contributions, while the warm-high pattern was associated with moderate BC concentration and small BC_{bb} contribution. The findings provide insights into the transport mechanisms of BC with the impacts of synoptic pattern in China.

1. Introduction

As an important component of atmospheric particulate matters, black carbon (BC) is throughout the Earth system (Bond et al., 2013). BC is emitted in variety of combustion-related processes of carbonaceous matters including fossil fuels, biofuels and biomass. Belonging to light-absorbing compounds, BC plays a vital role in the Earth's climate system since it can absorb solar radiation, affect cloud processes, and alter the melting of snow and ice cover (Ramanathan and Carmichael, 2008; Bond et al., 2013; Booth and Bellouin, 2015; Gustafsson and Ramanathan, 2016; Liu et al., 2019). BC can also change weather condition, affect pollution development and even contribute to extreme weather (Ding et al., 2013, 2016; Fan et al., 2015; Peng et al., 2016; Miao et al., 2019). In addition, BC influences air quality and atmospheric visibility (Bastien et al., 2015; Deng et al., 2016). Furthermore, BC is harmful to human health since it is mainly concentrated in the Aitken and accumulation mode and can adsorb many hazardous materials

* Corresponding author.
E-mail address: dengjunjun@tju.edu.cn (J. Deng).

https://doi.org/10.1016/j.chemosphere.2019.125133
0045-6535/

(Janssen et al., 2011; Nichols et al., 2013). Therefore, observations of BC with high temporal and spatial resolution are essential to improve our understanding on spatiotemporal distributions, transport characteristics and influencing mechanisms of BC and update our knowledge on its impacts on global environment and climate change.

BC largely contributed to air pollution, weather modification and climate change in China, which is with the largest emission of BC in the world (Zhuang et al., 2010; Wang et al., 2012; Andersson et al., 2015; Huang et al., 2016). During the past decade, field studies on temporal variations in BC concentration with high temporal resolution have been conducted in various regions in China including the Beijing-Tianjin-Hebei region (BTH) in North China, the Guanzhong Plain in Northwest China, the Yangtze River Delta region (YRD) in East China and the Pearl River Delta region (PRD) in South China (Cao et al., 2009; Wu et al., 2013; Zhuang et al., 2014; Shen et al., 2015; Liu et al., 2018). Cao et al. (2009) conducted two-year BC measurements with Aethalometer to examine temporal variations in BC in Xi'an in the Guangzhong Plain, and revealed a clear inverse relationship between BC and wind speed. Shallower mixed layer depths were also found during BC episodes. Wu et al. (2013) reported BC concentrations by Aethalometer and their variations on Yongxing Island in the South China Sea and at five continental sites in the PRD region in both rainy and dry seasons. Liu et al. (2018) measured BC concentration in Beijing during winter and analyzed the sources of BC during pollution episodes and clean days by Aethalometer. They found that BC was highly correlated with $PM_{2.5}$ (particulate matters with aerodynamic diameter $< 2.5\ \mu m$), and its concentration ranged from $0.17\ \mu g\ m^{-3}$ in clean days to $35.33\ \mu g\ m^{-3}$ in haze days. The widespread presence and large variability of BC call for BC observations with high spatiotemporal resolution. In addition to spatiotemporal variations in BC concentration, field study on regional originations and transport pathways of BC in China is becoming a hot issue in recent years (Cheng et al., 2006; Cheng et al., 2010; Guo et al., 2015; Wang et al., 2015). However, there is a lack of continuous study on BC in the Western Taiwan Strait region (WTS) in Southeast China, which is associated with better air quality comparing with other developed regions such as BTH, YRD and PRD because of the weaker emission and stronger diffusion. BC concentrations over background and remote regions with better air quality have been previously investigated. BC concentrations with their diurnal variations was analyzed at the Shangdianzi Global Atmosphere Watch (GAW) regional station (Yan et al., 2008). Continuous measurements of BC concentration were performed at the background site Prelia in Lithuania to characterize the BC distribution over the East Baltic region (Bycenkiene et al., 2011). Zhu et al. (2016) conducted BC measurements at Mt. Muztagh in the Western Tibetan Plateau to determine its seasonal variation, transport, and potential contribution source areas. Although with better air quality, WTS may be affected by air pollutants transported from the polluted regions under the impact of East Asian monsoon (Chen et al., 2013; Yan et al., 2016; Qiu et al., 2019). Therefore, it is essential to study on characteristics and regional transport of BC over WTS.

In the present study, continuous observations of BC in Xiamen in WTS were conducted. The objectives of this study are to characterize temporal variations in BC concentration and estimate the regional originations and potential transport pathways of BC. In particular, the impacts of synoptic circulation on BC emitted from different source sectors. The findings will improve our understanding on BC and its influencing mechanism in relatively clean region and provide scientific support to control BC pollution.

2. Methodologies

2.1. Observation site

With a population of ~4 million, Xiamen in Southeast China's coast (Fig. 1) is one of the five special economic zones in China. Qiu et al. (2019) found that in 2014 the prevailing wind in Xiamen was southeasterly in spring, southeasterly and southwesterly in summer, and northeasterly in autumn and winter. According to 2014 Report on the State of the Environment in China (available at http://www.mee.gov.cn/hjzl/zghjzkgb/lnzghjzkgb), in 2014, air quality in Xiamen ranked the eighth among the 74 large cities in China. According to the spatial distribution of BC emission (Li et al., 2017), Xiamen does not belong to the "hot spot" region. However, BC emitted from the "hot spot" regions such as YRD to the north and PRD to the southwest would transport to Xiamen under certain synoptic patterns.

The observation site is located at the Institute of Urban Environment, Chinese Academy of Sciences (118°03′E, 24°36′N) in Xiamen (Du et al., 2013; Deng et al., 2016). The site is ~15 km northwest from the downtown Xiamen. There is no big industrial sources within 10 km radius around the site. Only several roads and construction sites are around the site. The observation instruments were installed on the roof of a building with a height of ~8 m.

2.2. Instruments and measurements

One-year on-line observation of BC was carried out from Jan. 1 to Dec. 31 in 2014 by means of Aethalometer (AE31, Magee Scientific) with a $PM_{2.5}$ cut-off inlet. Using continuous filtration through a

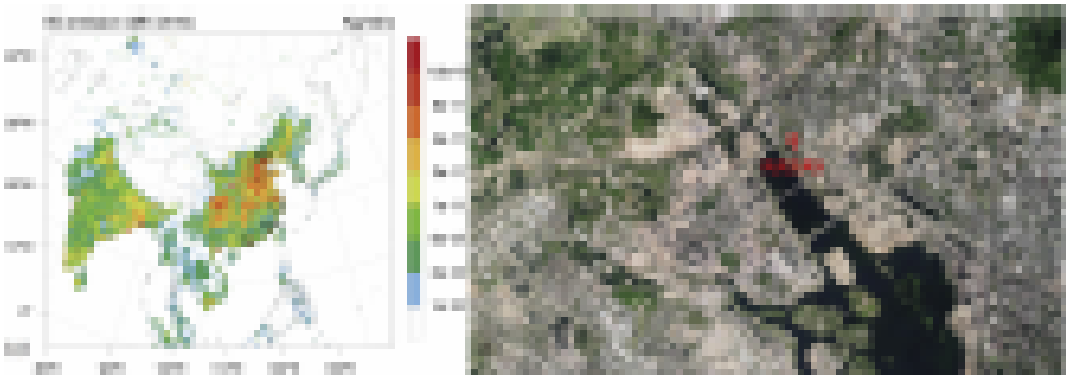

Fig. 1. (a) Location of Xiamen in China, with the spatial distribution of BC emission. The BC emission data are from the MIX inventory for 2010 (Li et al., 2017). Frame 1, Frame 2 and Frame 3 represent BTH, YRD and PRD, respectively. (b) Location of the observation site in Xiamen.

quartz filter, Aethalometer estimates absorbance of light from LED lamps (Hansen et al., 1984). The Aethalometer measured light absorbance at seven wavelengths (370, 470, 520, 590, 660, 880 and 950 nm) at a flow rate of 5 L min^{-1} and with a temporal resolution of 5 min. BC mass concentration was derived based on the light attenuation. BC measured at 880 nm is used to represent "true" ambient BC, since BC is the principal absorber of light at 880 nm and other light-absorbing organic compounds have negligible absorption (Ganguly et al., 2005). Although filter-based light absorption technique adopted in the AE31 Aethalometer has been widely used, it suffers from uncertainties in measurements of BC loading, which arises from shadowing effects and multiple scattering effects (Bond et al., 1999; Weingartner et al., 2003). Therefore, methods derived by Virkkula et al. (2007) were employed to correct BC concentration.

Mass concentration of $PM_{2.5}$ was synchronously measured by a Tapered Element Oscillating Microbalance (TEOM) sampler (RP1400, Thermo Fisher Scientific). Meteorological parameters, including wind speed/direction, temperature, pressure and precipitation, were automatically observed using the automatic weather station (MAWS301, Vaisala). Additionally, hourly convective planetary boundary layer height (PBLH) for 9:00–17:00 each day were estimated with the meteorological sounding data (http://www.weather.uwyo.edu/upperair/sounding.html) with the EPA AERMET model (Simpson et al., 2007) (Fig. S1).

2.3. Origination and transport pathways analysis

To identify the possible predominant directions of local sources relative to surface wind directions, the conditional probability function (CPF) (Ashbaugh et al., 1985) was calculated by using BC concentrations coupled with wind speed/direction. The CPF is defined as:

$$CPF_{\Delta\theta} = m_{\Delta\theta}/n_{\Delta\theta} \quad (1)$$

where $m_{\Delta\theta}$ is the number of occurrences from wind sector $\Delta\theta$ where the concentration exceeds the threshold criterion and $n_{\Delta\theta}$ is the total number of occurrence from the same wind sector. In this analysis, a threshold criterion of the upper 25% was chosen for BC concentrations (Lupu and Maenhaut, 2002; Bari and Kindzierski, 2017).

Origins and long-range transport of air masses arriving at Xiamen were investigated by three-dimensional backward trajectories with the Hybrid Single Particle Lagrangian Integrated Trajectory (HYSPLIT) model (Stein et al., 2015). 120 h backward trajectories reaching 500 m were modeled every hour. The input meteorological data of the model were from the Global Data Assimilation System (GDAS) reanalysis dataset with a spatial resolution of 1° (latitude) × 1° (longitude) and a temporal resolution of 6 h (available at ftp://arlftp.arlhq.noaa.gov/pub/archives/gdas1). The outputs of the model were hourly trajectory endpoints indicating the geographical location and the height of the air parcel. The backward trajectories were used to trace the outflow regimes for air masses and to identify the potential origins to the observation site. Cluster analysis was then implemented to obtain trajectory clusters.

Potential source contribution function (PSCF) model was applied to identify the predominant source distributions for long-range transporting BC with the obtained hourly backward trajectories. PSCF is a widely used method to identify regional sources based on the HYSPLIT model (Hopke et al., 1995; Bari et al., 2015; Sun et al., 2017). The zone of concern is divided into i × j small equal grid cells. The PSCF value for the ijth cell is defined as follows:

$$PSCF_{ij} = m_{ij}/n_{ij} \quad (2)$$

where n_{ij} is the total number of endpoints that fall in the ijth cell and m_{ij} is the number of endpoints for ijth cell that are associated with BC concentrations higher than an arbitrarily threshold criteria. Cells with high PSCF values are associated with the arrival of air masses with BC concentrations higher than the threshold. Therefore, these cells are the regions with high potential contributions to BC. In this analysis, the upper 25% of all the hourly concentration data was treated as the threshold (Lupu and Maenhaut, 2002; Bari and Kindzierski, 2017). The PSCF values were calculated over a geographical domain (10°–55° N and 80°–140° E) composing 10800 cells of 0.5° (latitude) × 0.5° (longitude).

Since cells can have the same PSCF value when concentrations are either slightly or much higher than the threshold, it is difficult for the PSCF model to distinguish moderate sources from strong ones. Therefore, the concentration-weighted trajectory (CWT) model was also performed to identify the originations and long-range transport of BC. In the CWT method, each cell is assigned a weighted concentration by averaging the sample concentrations that have associated trajectories that crossed the cell as follows (Hsu et al., 2003):

$$C_{ij} = \frac{1}{\sum_{l=1}^{M} \tau_{ijl}} \sum_{l=1}^{M} C_l \tau_{ijl} \quad (3)$$

where C_{ij} is the average weighted concentration in the ijth cell, M is the total number of trajectories, C_l is the BC concentration observed on arrival of trajectory l, and τ_{ijl} is the number of trajectory end points in the ijth cell associated with the C_l sample. In general, a high value for C_{ij} implies that air parcels traveling over the ijth cell would be associated with high concentrations at the receptor site.

The PSCF and CWT values were multiplied with an arbitrary weighting function w_{ij} to minimize the uncertainty in cells with small n_{ij} values (Polissar et al., 1999). w_{ij} was defined as follows:

$$w_{ij} = \begin{cases} 1.00 & n_{ij} > 3n_{ave} \\ 0.70 & 1.5n_{ave} < n_{ij} \le 3n_{ave} \\ 0.42 & n_{ave} < n_{ij} \le 1.5n_{ave} \\ 0.05 & n_{ij} \le n_{ave} \end{cases} \quad (4)$$

where n_{ave} was the average value of the endpoints per each cell.

2.4. Classification of synoptic circulation patterns

Synoptic circulations determine weather conditions such as wind speed/direction, precipitation, temperature and relative humidity. Therefore, synoptic circulation is crucial for transport, diffusion and deposition of air pollutants. Classification of synoptic circulations is often applied to categorize the impact of weather conditions on air pollutants and investigate the direct linkages between synoptic circulation and air quality (Zhang et al., 2012, 2013, 2016; Pope et al., 2015; Zheng et al., 2015; Bei et al., 2016; Liao et al., 2017).

In this work, semi-objective method combining the subjective and objective methods (Zhang et al., 2013) were applied to classify synoptic-scale circulations during 2014. Zheng et al. (2013) found that air quality in Xiamen was severely influenced by tropical cyclones. However, typhoons could not be identified well by the objective method due to their small size. Therefore, before the objective synoptic classification, two synoptic patterns associated with typhoon were subjectively classified by eyes: Typhoon I with the distance of the storm center to Xiamen less than 600 km, and Typhoon II with the distance of the storm center to Xiamen

between 600 and 1000 km.

Then, CKMEANS (k-means by dissimilar seeds) was adopted as the objective method, which is an optimization algorithm, based on the k-means clustering method (Philipp et al., 2010). In the CKMEANS classification, different from conventional k-means, a modified method was used for producing the dissimilar seeds for k-means clustering (Enke and Spekat, 1997). The objective classification was accomplished by utilizing Cost733class-1.2, which was a FORTRAN software package, including various methods for weather and circulation type classification (Philipp et al., 2014). Subjected to the objective recognition scheme, the 0000 UTC mean sea level pressure (MSLP) of the ERA-Interim reanalysis data (Dee et al., 2011) were used for the circulation typing calculation in this study. The data were with a grid resolution of $0.75° \times 0.75°$, covering the area between 20° and 35°N in latitude and between 110° and 125°E in longitude.

3. Results and discussion

3.1. Overview of BC concentration

Fig. 2 presents the seasonal normalized frequency distributions of hourly mean BC concentration, which all followed lognormal patterns. Throughout the entire period, hourly mean mostly less than 20000 ng m^{-3}. Over 70% and 94% of hourly BC concentrations were less than 5000 ng m^{-3} and 10000 ng m^{-3}, respectively. The maximum frequency of hourly BC concentration is 21.2% occurring in the range from 2000 to 3000 ng m^{-3}, followed by the frequency 17.0% in the range of 3000−4000 ng m^{-3} and 16.6% in the range of 1000−2000 ng m^{-3}. On a seasonal basis, the maximum frequencies of 22.6%, 21.1%, 22.2%, and 20.9% occurred at the ranges of 2000−3000 ng m^{-3}, 1000−2000 ng m^{-3}, 2000−3000 ng m^{-3}, and 2000−3000 ng m^{-3} in spring, summer, autumn, and winter, respectively. Percentage contribution of high hourly BC concentrations exceeding the annual mean were 43.1%, 34.8%, 41.6% and 34.4% in spring, summer, autumn and winter, respectively. Compared with other seasons, it is obvious that summer was the "BC trough" period with larger frequency of lower BC concentration while smaller frequency of higher BC concentration.

Fig. 3 shows the temporal variations of daily mean values of BC and $PM_{2.5}$ concentrations, BC/$PM_{2.5}$ fraction and meteorological variables such as PBLH, RH, wind speed/direction, temperature, pressure, and precipitation in Xiamen. Some observation data were missing due to the instrument maintenance.

Daily mean BC concentrations ranged from 779 to 12748 ng m^{-3}, and annual mean BC concentration was 4270 ± 1875 ng m^{-3} with >40% of the daily values exceeding the annual mean. The large temporal variability is closely related to variations in emission sources and meteorological conditions. The annual average BC/$PM_{2.5}$ fraction during 2014 was 11.9%, implying that BC was an important component in $PM_{2.5}$ in Xiamen. The contribution of BC to $PM_{2.5}$ in Xiamen was much higher than that in Shanghai (5.3%) (Zha et al., 2014) and Xi'an (8.3%) (Cao et al., 2009) in China and Anantapur (4.6%) (Reddy et al., 2012) and Delhi (5.3%) (Tiwari et al., 2013) in India, indicating the greater importance of light-absorbing aerosols and the different characteristics of aerosol pollution in the coastal city.

BC concentrations measured by Aethalometer in different locations around the world are summarized in Table 1. BC concentration in Xiamen was mostly comparable or lower than that obtained in urban or suburban areas in China, such as Beijing (Liu et al., 2018), Guangzhou (Wu et al., 2013), Dongguan (Wu et al., 2013), Nanjing (Zhuang et al., 2014), Jiaxing (Shen et al., 2015), Xianghe (Ran et al., 2016) and Xi'an (Cao et al., 2009). However, the level was higher than that in most rural, coastal and background areas in China, such as Shangdianzi (Yan et al., 2008), Tongyu (Cheng et al., 2010) and Tibetan Plateau (Zhu et al., 2016). Moreover, BC concentration in Xiamen was higher than that in the USA (Watson and Chow, 2002), France (Healy et al., 2012), Italy (Mousavi et al., 2019), UK (Reche et al., 2011), Lithuania (Bycenkiene et al., 2011) and Athens (Kalogridis et al., 2018). Nevertheless, it was lower than that in India (Tiwari et al., 2013; Joshi et al., 2016; Vaishya et al., 2017) and Pakistan (Husain et al., 2007) in South Asia that is one of the largest emission zones of BC in the world (Fig. 1).

3.2. Temporal variations in BC concentration

Monthly and diurnal variations in BC concentration were depicted in Fig. 4. The high concentrations during the campaign mainly occurred in 5:00−7:00 in August, while the low concentrations were mainly distributed in 12:00−16:00 in June−July. BC concentration exhibited a pronounced diurnal pattern. Increasing steadily before dawn, BC reached its peak at 6:00 in the early morning with a value of 6182 ng m^{-3}. Then, it decreased gradually and reached the diurnal minimum value of 2847 ng m^{-3} at 13:00 in the afternoon. The diurnal pattern of BC in Xiamen was similar with

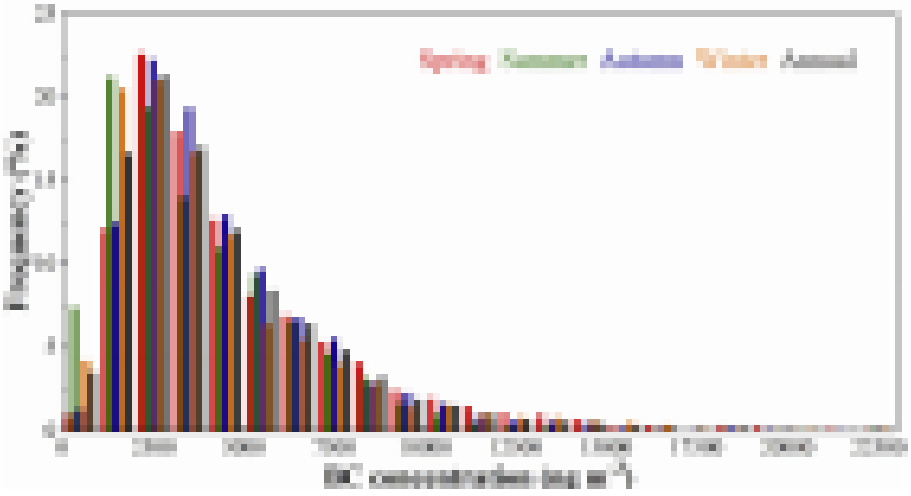

Fig. 2. Frequency distributions of hourly mean BC concentration in Xiamen in 2014.

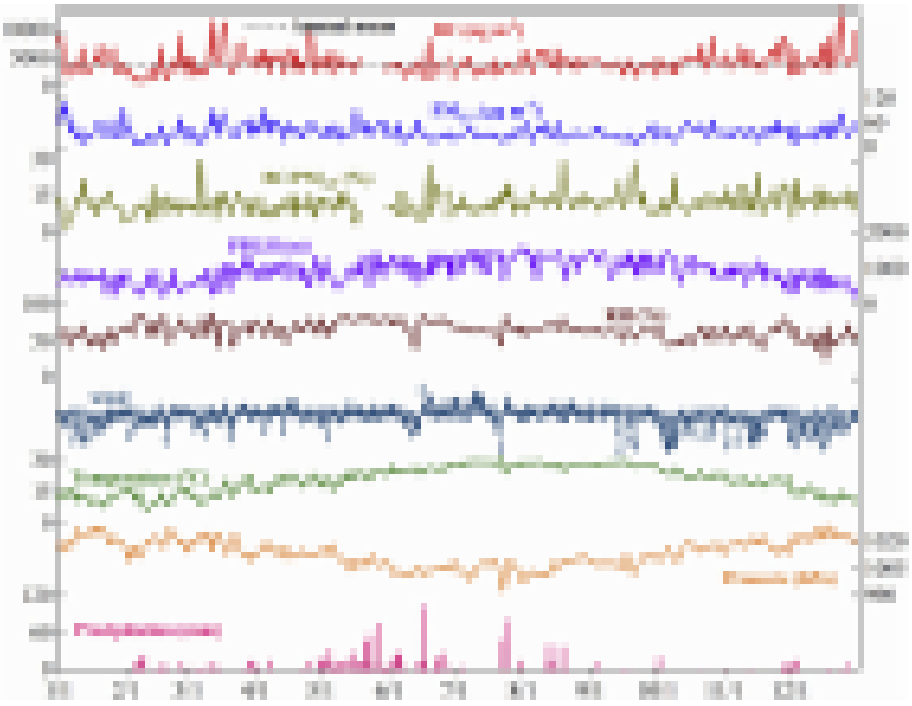

Fig. 3. Time series of daily BC, $PM_{2.5}$, $BC/PM_{2.5}$ fraction, PBLH, RH, wind, temperature, pressure, and precipitation in Xiamen in 2014.

Table 1
Comparisons of BC concentrations measured with Aethalometer at different locations.

Observation site	Site type	Period	Concentration	Reference
Xiamen, China	Urban	2014	4270 ng m^{-3}	This study
Dongguan, China	Suburban	2008.5–6	4.86 μg m^{-3}	Wu et al. (2013)
Guangzhou, China	Suburban	2008.5–6	5.57 μg m^{-3}	Wu et al. (2013)
		2008.12–2009.1	7.68 μg m^{-3}	
Xi'an, China	Suburban	2003.9–2005.8	14.7 μg m^{-3}	Cao et al. (2009)
Taicang, China	Suburban	2005.5–6	5.47 μg m^{-3}	Zhou et al. (2009)
Athens, Greece	Suburban	2014.12–2015.3	2655 ng m^{-3}	Kalogridis et al. (2018)
Bareggio, Italy	Suburban	2017–2018	2763 ng m^{-3}	Mousavi et al. (2019)
Pantnager, India	Suburban	2009–2012	5.5 μg m^{-3}	Joshi et al. (2016)
Beijing, China	Urban	2015.12–2016.2	5.31 μg m^{-3}	Liu et al. (2018)
Shanghai, China	Urban	2010	3.8 μg m^{-3}	Feng et al. (2014)
		2011	3.3 μg m^{-3}	
Shanghai, China	Urban	2011.1–2012.1	2.33 μg m^{-3}	Zha et al. (2014)
Nanjing, China	Urban	2012	4157 ng m^{-3}	Zhuang et al. (2014)
Jiaxing, China	Urban	2013.9–11	5.1 μg m^{-3}	Shen et al. (2015)
Xianghe, China	Urban	2014.4–2015.3	4.93 μg m^{-3}	Ran et al. (2016)
Guangzhou, China	Urban	2008.5–6	8.86 μg m^{-3}	Wu et al. (2013)
		2008.12–2009.1	20.21 μg m^{-3}	
Fresno, USA	Urban	2000	1.17 μg m^{-3}	Watson and Chow (2002)
Lahore, Pakistan	Urban	2005.11–2006.1	21.7 μg m^{-3}	Husain et al. (2007)
New Delhi, India	Urban	2007	6.7 μg m^{-3}	Tiwari et al. (2013)
Gorakhpur, India	Urban	2013.8	8–28 μg m^{-3}	Vaishya et al. (2017)
London, UK	Urban	2009	1.9 μg m^{-3}	Reche et al. (2011)
Paris, France	Urban	2010.1–2	1.66 μg m^{-3}	Healy et al. (2012)
Milan, Italy	Urban	2017–2018	1921 ng m^{-3}	Mousavi et al. (2019)
Shangdianzi, China	Rural	2003.4–2005.1	2.12 μg m^{-3}	Yan et al. (2008)
Changping, China	Rural	2005.6–7	2.37 μg m^{-3}	Zhou et al. (2009)
Silinhot, China	Rural	2005.4	2 μg m^{-3}	Niu and Zhang (2010)
		2005.12	6.2 μg m^{-3}	
Tongyu, China	Rural	2008	2.52 μg m^{-3}	Cheng et al., 2010
Xinken, China	Rural	2008.12–2009.1	12.61 μg m^{-3}	Wu et al. (2013)
Hong Kong, China	Coastal	2004.6–2005.5	2.4 μg m^{-3}	Cheng et al. (2006)
Prelia, Lithuania	Coastal	2008–2009	0.6 μg m^{-3}	Bycenkiene et al. (2011)
Tibetan Plateau, China	Background	2009.11–2010.9	133 ng m^{-3}	Zhu et al. (2016)

that found in some other cities (Zhou et al., 2009; Zhuang et al., 2014; Joshi et al., 2016). Such diurnal cycles reflect the combined effect of the dial BC emission trends, variation in surface meteorology and the associated boundary layer dynamics (Srivastava

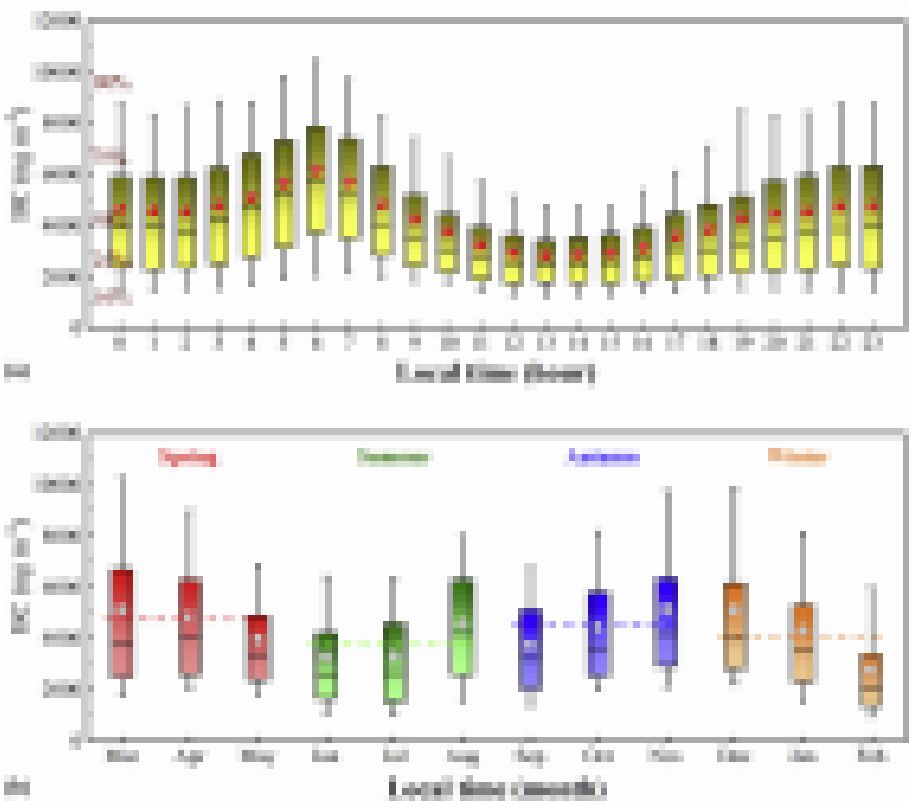

Fig. 4. (a) Monthly and (b) diurnal variations in BC concentration in Xiamen in 2014.

et al., 2012; Tiwari et al., 2013; Zhuang et al., 2014). The early morning peak was mainly resulted from entrainment of BC from the nocturnal residual layer and morning anthropogenic activities such as the elevated vehicle emissions during the traffic rush hours. After the morning peak, the boundary layer gradually developed and surface temperature increased. As shown in Fig. S1a, the boundary layer was much higher at 17:00 than that in 9:00 by a factor of about three. This would enhance vertical/horizontal diffusion of pollutants and lead to the steady decrease in BC concentration. From the late afternoon to night, due to the decrease in boundary layer height and turbulent mixing, air pollutants including BC were accumulated in the lower surface layer, leading to relatively high BC concentration from midnight to early morning. Additionally, the sea-land breeze circulation around the coastal region might contribute to such diurnal variation. Land breeze from the continent at night brought in BC-rich continental air, and consequently improved the BC concentration. However, sea breeze in the daytime brought in marine air, which was rather free from BC since there were no sources of BC over the sea. This led to a remarkable decrease in BC concentration and it remained low during the sea-breeze regime (Babu and Moorthy, 2001).

The highest monthly mean BC concentration was recorded in November (5179 ng m^{-3}) and the lowest was in February (2806 ng m^{-3}). An evident variation on seasonal time scale in BC concentration was found with the mean concentrations showing a sequence in magnitude: spring (March–May 4755 ng m^{-3}) > autumn (September–November 4466 ng m^{-3}) > winter (December–January 4136 ng m^{-3}) > summer (June–August 3774 ng m^{-3}). The seasonal pattern of BC in Xiamen, namely low in summer and high in spring, autumn and winter, was similar to the state of other cities over China including Xi'an (Cao et al., 2009), Nanjing (Zhuang et al., 2014), Hong Kong (Cheng et al., 2006) and Tongyu (Cheng et al., 2010). Seasonal variations in BC concentration were also affected by both source emissions and meteorological conditions. Coal burning is China's largest energy source. In summer, temperature is overall high (Fig. 3), and therefore the energy consumption from coal burning is lower than other seasons. According to Li et al. (2017), anthropogenic BC emission from fossil fuel in China was lower in summer and higher in winter, which could lead to low BC loading in summer while high BC loading in winter. The lowest BC level in February might be due to the reduced emissions from traffic exhausts and domestic cooking or heating in local or the surrounding areas during the long traditional Chinese Holiday-Spring Festival. Besides anthropogenic emissions, meteorological parameters are important factors controlling the BC level. Meteorological conditions in summer including higher temperature, more rainfall and larger PBLH (Fig. 3 and Fig. S1b) are beneficial to diffusion and scavenging of air pollutants, contributing to the lower summertime BC concentration. Impacts of meteorological parameters including precipitation and wind on BC will be briefly discussed in Section 2 in the supplementary materials. Additionally, under the control of summer monsoon, less air pollutants transporting from the polluted areas in northern and eastern China also resulted in the lower BC level. Impact of long-range transport on BC concentration will be discussed in Section 3.3.

3.3. Sources and transport pathways in relation to high BC concentrations

The CPF analysis result for BC concentration using the upper 25% thresholds (5481 ng m^{-3}) is depicted in Fig. 5. For local (short-range) point source contributions, the CPF plot of BC indicates northwest, north and northeast as dominant directions. High BC

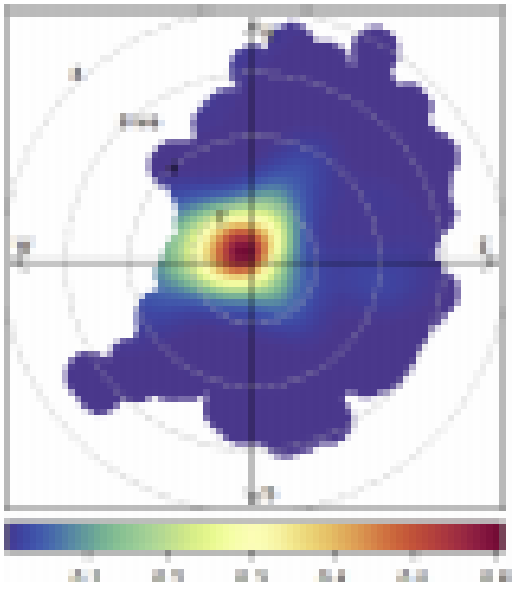

Fig. 5. CPF plots for BC in Xiamen in 2014. ws represents wind speed (m s^{-1}).

concentrations were mainly affected by winds ranging from west-southwest to north-northeast with higher values associated with wind speeds lower than 2 m s^{-1}. BC concentration was highest with winds from the northwest at low wind speed (<~1.5 m s^{-1}) and to a lesser extent from the west and north-northeast at moderate wind speed (<3 m s^{-1}). The BC plot suggests local sources such as the traffic emissions to the northwest of the site within a short distance.

The long-range transport of air masses were identified with the HYSPLIT model. Transport pathways with four clusters were further obtained by the clustering analysis and the cluster-mean trajectories are depicted in Fig. 6. The first cluster (C1) is the northeastern coastal cluster originating from the East China Sea and passing along with East China Coast region and some relative inland areas. The second cluster (C2) is the southwestern marine cluster passing through the South China Sea. The third cluster (C3) originating from Mongolia and the fourth cluster (C4) originating from Siberia are two long-range inland clusters passing through the heavily polluted areas such as North China Plain and YRD. C1, C2, C3 and C4 contributed to 47.1%, 21.4%, 23.2% and 8.2% of the total air masses, respectively. The northeastern coastal cluster C1 had the highest BC concentration (4528 ± 3204 ng m^{-3}). BC concentration of marine clusters passing through the South China Sea (C2) was 4077 ± 2736 ng m^{-3}, even higher than that of the inland cluster C4. It was because of the strong influence of air pollution in the atmospheric boundary layer or near surface on the marine clusters C1 and C2 due to the weak vertical transport (Qiu et al., 2019). The inland clusters C3 and C4, which passed through North China and East China, were associated with BC concentrations of 4181 ± 2758 ng m^{-3} and 3548 ± 2257 ng m^{-3}, respectively.

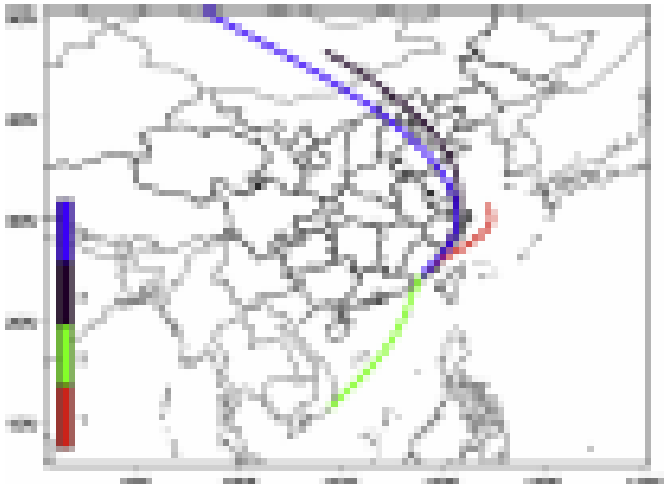

Fig. 6. Cluster-mean of the five-day backward trajectories at 500 m elevation in Xiamen.

The PSCF and CWT analyses were further conducted to identify potential sources and their contributions to the receptor sites by combining the backward trajectories and corresponding hourly BC concentration data. Spatial distribution of potential source regions of BC in Xiamen is illustrated in Fig. 7a. Based on the PSCF maps, many potential sources for BC with high PSCF values (PSCF>0.4) were located in the surrounding regions and to the southwest of Xiamen, including Longyan and Zhangzhou in Southwest Fujian province, Guangzhou and Huizhou in East Guangdong province. Significant potential sources also distributed in the provinces (Hubei, Hunan and Jiangxi) in east-central China on the northwest terrestrial side of Xiamen, which belonged to the major zone of BC emission in China. It indicates that long-range sources significantly contributed to BC in Xiamen. East China Sea to the east and South China Sea to the southwest were also identified as the potential source regions likely due to the trailing effect (Lee et al., 2014; Feng et al., 2015; Zhang et al., 2017) and the heavy commercial shipping traffic in the coastal waters (Wang et al., 2016).

Fig. 7b shows the distribution of the weighted trajectory concentrations of BC obtained from the CWT analysis, which provides information on the relative contributions of potential sources regions to BC concentration in Xiamen. The CWT results were similar to the results found using the PSCF method. In addition to the surrounding areas, exogenous sources of BC were mainly localized to Anhui and Jiangxi provinces in east-central China to the northwest, the South China Sea to the southwest and the East China Sea to the east, with high CWT values of >5000 ng m^{-3}. Central and western China, including Shaanxi, Chongqing, Hubei and Henan provinces, had CWT values of >3000 ng m^{-3}. Guangxi province in China and Vietnam, Laos, Cambodia and Thailand in Southeast Asia also contributed significantly to BC concentration (with CWT values of >2000 ng m^{-3}) in Xiamen.

3.4. Impacts of synoptic circulation on BC from different source sectors

Based on the semi-objective method, synoptic-scale circulations affecting Xiamen in 2014 were classified into nine prevailing circulation types (CTs). The composite MSLP maps along with the occurrence frequencies for the nine predominant CTs are depicted in Fig. 8. Meteorological parameters and weather conditions of the nine CTs are summarized in Table 2. The occurrence frequency of each CT for the four seasons are presented in Table S1. CT6 and CT4 occurred more frequently in spring. CT2 was predominant in summer, followed by CT4. For autumn, the predominant patterns were CT1 and CT5, while the major patterns were CT7, CT3 and CT5 for winter. According to the MSLP distributions, the nine CTs can be further defined as cyclone-related patterns and anticyclone-related patterns. The former included CT2, CT8 and CT9, and the latter included the other patterns.

To investigate the impacts of synoptic circulation on BC from different source sectors, BC was divided into BC from combustion of fossil fuel (BC_{ff}) and BC from biomass burning (BC_{bb}).

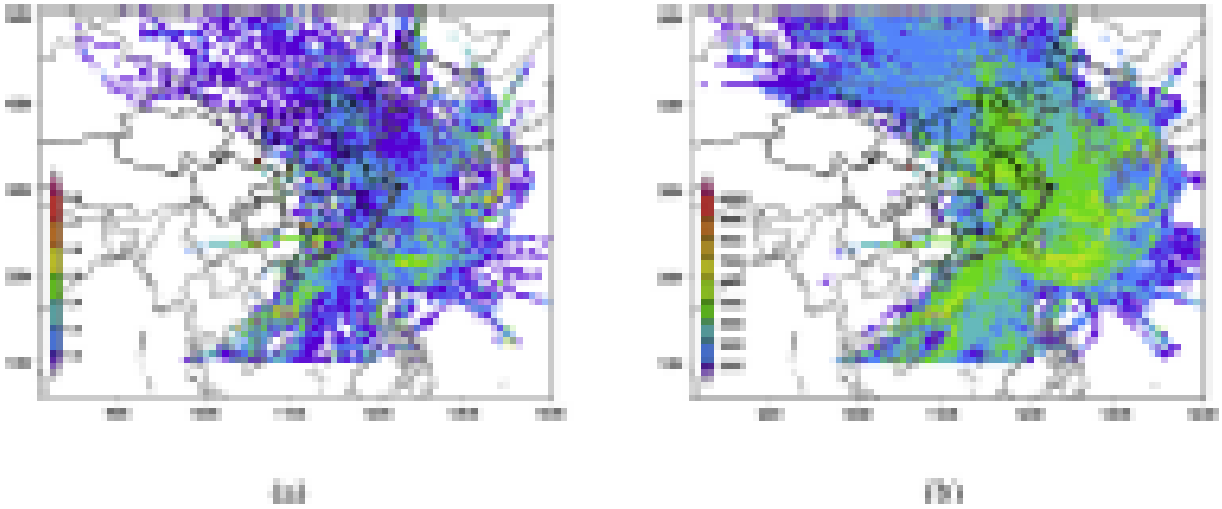

Fig. 7. (a) PSCF and (b) CWT (ng m^{-3}) maps for BC in Xiamen in 2014.

Concentrations of BC_{ff} and BC_{bb} were calculated with the "Aethalometer model" (Sandradewi et al., 2008). The "Aethalometer model" is briefly described in Section 4 in the supplementary materials. Mean BC, BC_{ff} and BC_{bb} concentrations with the BC_{bb} contribution to BC under the influence of each CT are presented in Fig. 9.

CT8 (Typhoon I) and CT9 (Typhoon II) were two typical Typhoon-related weather circulation patterns and mainly occurred from late spring to early autumn, contributing 3.8% and 4.4% to all days, respectively. In the pattern of CT8, Xiamen was right influenced by a moving tropical cyclone and the center of the cyclone was over the South China Sea and to the south of Fujian province in China. However, in CT9 Xiamen was on the periphery of a tropical cyclone, and the center of the cyclone was over the north of Philippines. Consequently, Xiamen was more likely affected by spiral rain bands and stronger wind of the typhoon in CT8 and was more frequently influenced by the downdraft in CT9 with less precipitation and more stable conditions. As a result, CT8 was associated with the lowest concentrations of BC (3119 ng m^{-3}), BC_{ff} (2078 ng m^{-3}) and BC_{bb} (1042 ng m^{-3}) due to the largest precipitation amount (19.5 mm) and higher wind speed (2.1 m s^{-1}). Because of the smaller precipitation amount (0.9 mm) in CT9, concentrations of BC, BC_{ff} and BC_{bb} were 3584 ng m^{-3}, 2360 ng m^{-3} and 1225 ng m^{-3}, respectively, higher than those in CT8. However, the biomass burning contribution to BC in CT9 was 35.2%, which was comparable with BC_{bb} contribution (34.7%) in CT8. Another cyclone-related synoptic pattern was CT2. CT2 mainly occurred in summer and accounted for 13.0% of total days. Under the influence of CT2, Xiamen was affected by southerly flows introduced by low-pressure systems or tropical cyclone. Circulation characteristics of CT2 were associated with a trough extended over South China or the South China Sea with its axis oriented from west to east (Zhang et al., 2013). The CT2-related meteorological conditions were low wind speed (1.1 m s^{-1}), high temperature (27.4 °C) and moderate precipitation amount (4.2 mm). Since Xiamen was usually influenced by clean air masses from the South China Sea, CT2 was associated with a relatively low BC concentration (3859 ng m^{-3}) and the smallest biomass burning contribution (29.3%). In short, under the influence of the three cyclone-related circulation patterns, Xiamen was associated with low BC concentrations (3663 ng m^{-3}) and small biomass burning contributions (30.3%).

Circulation patterns CT7, CT3 and CT5 were typical anticyclone synoptic patterns with cold-high system mainly occurring in winter. Circulation characteristics of the three patterns were determined by winter monsoon. CT7 accounted for 12.2% of the total number of days. In CT7, the high-pressure system centered over Northwest China and covered the central and eastern China, which introduced cold dry outflow from mainland China. Xiamen was affected by air masses from northeast, with the BC concentration of 4107 ng m^{-3}. Since the airflows in CT7 passed through the regions with densely biomass burning, the BC_{bb}/BC percentage (38.8%) under the influence of CT7 was relatively high. CT3 when continental cold high moved eastward and centered over North China accounting for 6.7% of all days. In CT3, air mass blew over the East China Sea and the Taiwan Strait and traveled along the coastline of Southeast China. Under the influence of CT3, Xiamen was in the bottom of anticyclone and affected by northeasterly cold dry wind. As a result, BC concentration in Xiamen was 4132 ng m^{-3}, with the largest biomass burning contribution (43.8%). CT5 with the second largest contributions of 15.4% to all days was associated with cold high centering over East China. Because of the impact of CT5, weather condition in Xiamen would be sunny with increasing temperature and northeasterly airflow. Average BC concentration in CT5 was 4234 ng m^{-3} with a relatively large biomass burning contribution of 36.6%. Overall, the three cold-high circulations were associated with moderate BC concentrations (4233 ng m^{-3}) and large biomass burning contributions (36.5%).

Circulation pattern on the largest number of days was CT4, which contributed for 16.3% of all days and mainly occurred in the transitional seasons from late spring to early autumn. Under the influence of CT4, Xiamen was controlled by the edge of warm high system, which covered South China and Southeast China. CT4 usually introduced stable weather condition with the lowest mean wind speed (0.9 m s^{-1}), high temperature (26.5 °C) and relatively large precipitation amount (6.0 mm). Moderate BC concentration (4020 ng m^{-3}) was found to be associated with CT4. However, the biomass burning contribution (31.0%) was small under CT4 since the prevailing wind was southerly.

CT1 and CT6 were anticyclone circulations, which mainly occurred in spring and autumn. CT1 when the continental cold high centered over central and eastern China contributed 14.5% to all days. In CT1, Xiamen was controlled by the cold high and affected by easterly wind with low wind speed (1.1 m s^{-1}). BC concentration under the CT1 pattern was the highest (5214 ng m^{-3}) with a moderate biomass burning contribution (32.6%) due to the stable weather conditions. CT6 with the center of high-pressure system

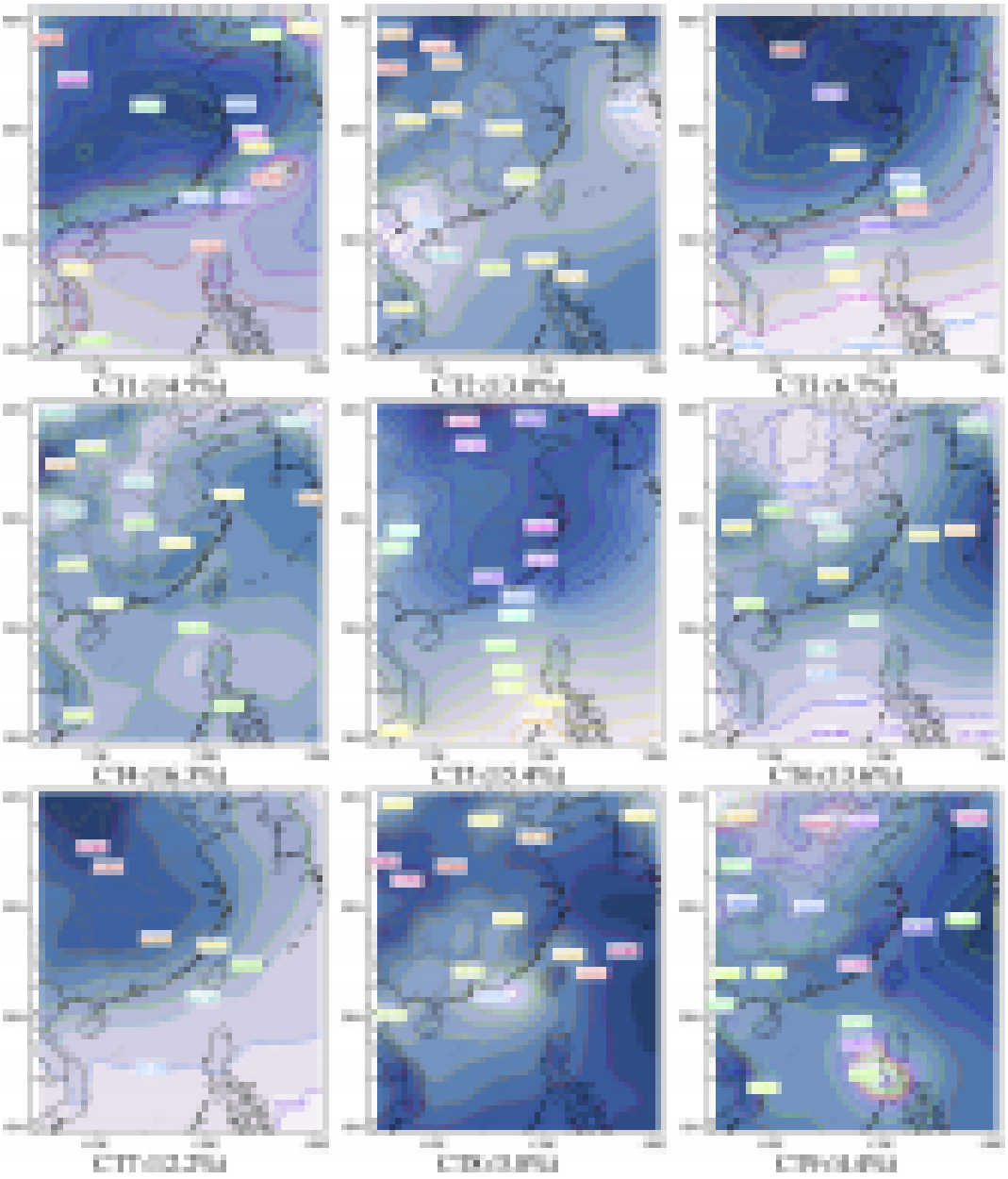

Fig. 8. MSLP patterns and occurrence frequency (bottom number) for each circulation type in 2014.

over the sea accounted for 13.6% of the total number of days. Being in front of the trough and behind the ridge, Xiamen was affected by easterly wind with low wind speed in CT6. Under the influence of CT6, Xiamen was associated with the second highest BC concentration 4559 ng m^{-3} and a low BC_{bb}/BC ratio of 30.4%. In a word, with the impact of the two anticyclone circulation patterns, Xiamen had high BC concentrations (4896 ng m^{-3}) and small biomass burning contributions (29.6%).

4. Conclusions

In this study, we performed one-year continuous measurements of BC aerosol with an Aethalometer in Xiamen in 2014. Temporal variations and transport pathways of BC were analyzed. Impacts of synoptic circulation on BC from different source sectors were also investigated.

Annual mean BC concentration in Xiamen in 2014 was 4270 ± 1875 ng m^{-3}. BC exhibited a pronounced diurnal variation with the maximum of 6182 ng m^{-3} at 6:00 and minimum of 2847 ng m^{-3} at 13:00. An evident seasonal variation existed with the maximum of 4755 ng m^{-3} in spring and minimum of 3774 ng m^{-3} in summer. CPF analysis suggested that high BC concentrations were associated with northwesterly winds with low wind speed and westerly and north-northeasterly winds with moderate wind speed. Northerly wind with high wind speed and east-northeasterly wind frequently led to large biomass burning contribution.

Air masses originating from the East China Sea and passing along with East China Coast region had the highest BC (4528 ng m^{-3}) concentration. PSCF and CWT analysis showed that the surrounding region, southwestern Fujian and eastern Guangdong to the southwest and Hubei, Hunan and Jiangxi to the northwest were major sources of BC. The East China Sea and South China Sea were also important source regions of BC.

Table 2
Corresponding meteorological parameters and weather conditions of the nine circulation types.

Type	PWD	MWS (m/s)	PRC (mm)	MAT (°C)	MRH (%)	Weather Conditions
CT1	E	1.1	1.9	19.6	66	(1) Mainly in spring and autumn and Xiamen is controlled by continental cold high; (2) Affected by easterly wind with small wind speed.
CT2	S	1.1	4.2	27.4	70	(1) Mainly in summer and Xiamen is controlled by low-pressure system; (2) Affected by southerly wind with more cloud and precipitation.
CT3	NE	2.2	0	11.7	50	(1) Mainly in winter; (2) Cold high is located in the north of China, and Xiamen is in the bottom of cold high; (3) Affected by northeasterly wind and weather is dry and cold.
CT4	S	0.9	6.0	26.5	72	(1) Mainly in from late spring to early autumn; (2) Affected by the warm high with small wind speed.
CT5	NE	1.5	1.5	16.2	62	(1) Cold high is in East China; (2) Xiamen will be sunny with increasing air temperature
CT6	E	1.1	2.5	22.4	68	(1) Mainly in spring and autumn; (2) Center of high pressure over the sea, Xiamen is in front of the trough and behind the ridge; (3) Cloudy and affected by easterly wind with small wind speed.
CT7	NE	1.8	1.2	14.1	60	(1) Mainly in winter; (2) High pressure in Northwest China, Xiamen is affected by air masses from northeast.
CT8	Variable	2.1	18.5	27.6	66	(1) Mainly in summer and autumn and typhoon is within the range of less than 600 km; (2) With high wind speed and increasing cloudiness, precipitation is easy to occur.
CT9	Variable	1.5	0.9	28.6	59	(1) Mainly in summer and spring and typhoon is within the range of 600−1000 km; (2) Weather condition is stable with little precipitation.

PWD: Prevailing Wind Direction; MWS: Mean Wind Speed; PRC: Precipitation; MAT: Mean Air Temperature; MRH: Mean Relative Humidity.

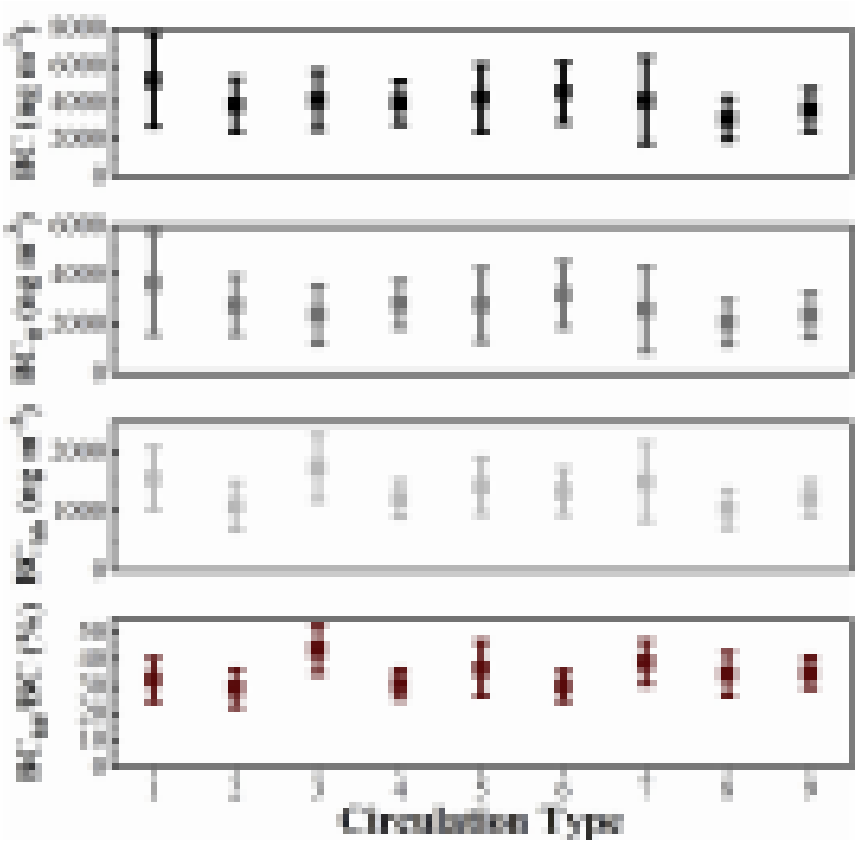

Fig. 9. Mean BC, BC_{ff} and BC_{bb} concentrations (ng m^{-3}) and BC_{bb}/BC fraction (%) during the nine circulation types in 2014.

Nine typical synoptic-scale circulation types affecting Xiamen including three cyclone-related patterns and six anticyclone-related patterns were identified with a semi-objective classification method. The cyclone-related circulation patterns were associated with low BC concentrations (3663 ng m^{-3}) and small biomass burning contributions (30.3%). Of the six anticyclone-related patterns, the three cold-high circulations around winter were associated with moderate BC concentrations (4233 ng m^{-3}) and large biomass burning contributions (36.5%), while the two cold-high patterns in spring and autumn were associated with high BC concentrations (4896 ng m^{-3}) and small biomass burning contributions (29.6%). Besides, under the influence of the warm-high pattern, Xiamen was moderate BC concentration (4020 ng m^{-3}) and small biomass burning contribution (31.0%).

Acknowledgments

This study was supported by National Natural Science Foundation of China (21607148, 41807309). The authors gratefully appreciate the provision of the HYSPLIT model from the NOAA/ARL.

Appendix A. Supplementary data

Supplementary data to this article can be found online at https://doi.org/10.1016/j.chemosphere.2019.125133.

Declaration of interests

The authors declare that they have no known competing financial interests or personal relationships that could have appeared to influence the work reported in this paper.

References

Andersson, A., Deng, J., Du, K., Zheng, M., Yan, C., Skold, M., Gustafsson, O., 2015. Regionally-varying combustion sources of the January 2013 severe haze events over Eastern China. Environ. Sci. Technol. 49, 2038–2043.

Ashbaugh, L.L., Malm, W.C., Sadeh, W.Z., 1985. A residence time probability analysis of sulfur concentrations at Grand Canyon National Park. Atmos. Environ. 19, 1263–1270.

Babu, S.S., Moorthy, K.K., 2001. Anthropogenic impact on aerosol black carbon mass concentration at a tropical coastal station: a case study. Curr. Sci. 81 (8), 1208–1214.

Bari, M.A., Kindzierski, W.B., Wallace, L.A., Wheeler, A.J., MacNeill, M., Heroux, M.E., 2015. Indoor and outdoor levels and sources of submicron particles (PM_1) at homes in Edmonton, Canada. Environ. Sci. Technol. 49, 6419–6429.

Bari, M.A., Kindzierski, W.B., 2017. Characteristics of air quality and sources affecting fine particulate matter ($PM_{2.5}$) levels in the City of Red Deer, Canada. Environ. Pollu. 221, 367–376.

Bastien, L.A.J., McDonald, B.C., Brown, N.J., Harley, R.A., 2015. High-resolution mapping of sources contributing to urban air pollution using adjoint sensitivity analysis: benzene and diesel black carbon. Environ. Sci. Technol. 49 (12), 7276–7284.

Bei, N., Li, G., Huang, R.J., Cao, J., Meng, N., Feng, T., Liu, S., Zhang, T., Zhang, Q., Molina, L.T., 2016. Typical synoptic situations and their impacts on the wintertime air pollution in the Guanzhong basin, China. Atmos. Chem. Phys. 16, 7373–7387.

Bond, T.C., Anderson, T.L., Campbell, D., 1999. Calibration and intercomparison of filter-based measurements of visible light absorption by aerosols. Aerosol Sci. Technol. 30, 582–600.

Bond, T.C., Doherty, S.J., Fahey, D.W., Forster, P.M., Berntsen, T., DeAngelo, B.J., Flanner, M.G., Ghan, S., Kärcher, B., Koch, D., Kinne, S., Kondo, Y., Quinn, P.K., Sarofim, M.C., Schultz, M.G., Schulz, M., Venkataraman, C., Zhang, H., Zhang, S., Bellouin, N., Guttikunda, S.K., Hopke, P.K., Jacobson, M.Z., Kaiser, J.W., Klimont, Z., Lohmann, U., Schwarz, J.P., Shindell, D., Storelvmo, T., Warren, S.G., Zender, C.S., 2013. Bounding the role of black carbon in the climate system: a scientific assessment. J. Geophys. Res.-Atmos. 118, 5380–5552.

Booth, B., Bellouin, N., 2015. Black carbon and atmospheric feedbacks. Nature 519, 167–168.

Bycenkiene, S., Ulevicius, V., Kecorius, S., 2011. Characteristics of black carbon aerosol mass concentration over the East Baltic region from two-year measurements. J. Environ. Monit. 13, 1027–1038.

Cao, J.J., Zhu, C.S., Chow, J.C., Watson, J.G., Han, Y.M., Wang, G.H., Shen, Z.X., An, Z.S., 2009. Black carbon relationships with emissions and meteorology in Xi'an, China. Atmos. Res. 94, 194–202.

Chen, B., Andersson, A., Lee, M., Kirillova, E.N., Xiao, Q., Krusa, M., Shi, M., Hu, K., Lu, Z., Streets, D.G., Du, K., Gustafsson, O., 2013. Source forensics of black carbon aerosols from China. Environ. Sci. Technol. 47 (16), 9102–9108.

Cheng, T., Han, Z., Zhang, R., Du, H., Jia, X., Wang, J., Yao, J., 2010. Black carbon in a continental semi-arid area of Northeast China and its possible sources of fire emission. J. Geophys. Res. 115 (D23204) https://doi.org/10.1029/2009JD13523.

Cheng, Y., Lee, S.C., Ho, K.F., Wang, Y.Q., Cao, J.J., Chow, J.C., Watson, J.G., 2006. Black carbon measurement in a coastal area of south China. J. Geophys. Res. 111 (D12310) https://doi.org/10.1029/2005jd006663.

Dee, D.P., Uppala, S.M., Simmons, A.J., Berrisford, P., Poli, P., Kobayashi, S., Andrae, U., Balmaseda, M.A., Balsamo, G., Bauer, P., Bechtold, P., Beljaars, A.C.M., van de Berg, L., Bidlot, J., Bormann, N., Delsol, C., Dragani, R., Fuentes, M., Geer, A.J., Haimberger, L., Healy, S.B., Hersbach, H., Hólm, E.V., Isaksen, L., Kållberg, P., Köhler, M., Matricardi, M., McNally, A.P., Monge-Sanz, B.M., Morcrette, J.J., Park, B.K., Peubey, C., de Rosnay, P., Tavolato, C., Thépaut, J.N., Vitart, F., 2011. The ERA-Interim reanalysis: configuration and performance of the data assimilation system. Q. J. Roy. Meteor. Soc. 137 (656), 553–597.

Deng, J., Zhang, Y., Hong, Y., Xu, L., Chen, Y., Du, W., Chen, J., 2016. Optical properties of $PM_{2.5}$ and the impacts of chemical compositions in the coastal city Xiamen in China. Sci. Total Environ. 557–558, 665–675.

Ding, A.J., Huang, X., Nie, W., Sun, J.N., Kerminen, V.M., Petaja, T., Su, H., Cheng, Y.F., Yang, X.Q., Wang, M.H., Chi, X.G., Wang, J.P., Virkkula, A., Guo, W.D., Yuan, J., Wang, S.Y., Zhang, R.J., Wu, Y.F., Song, Y., Zhu, T., Zilitinkevich, S., Kulmala, M., 2016. Enhanced haze pollution by black carbon in megacities in China. Geophys. Res. Lett. 43 (6), 2873–2879.

Ding, A.J., Fu, C.B., Yang, X.Q., Sun, J.N., Petaja, T., Kerminen, V.M., Wang, T., Xie, Y., Herrmann, E., Zheng, L.F., Nie, W., Liu, Q., Wei, X.L., Kumala, M., 2013. Intense atmospheric pollution modifies weather: a case of mixed biomass burning with fossil fuel combustion pollution in eastern China. Atmos. Chem. Phys. 13, 10545–10554.

Du, K., Mu, C., Deng, J., Yuan, F., 2013. Study on atmospheric visibility variations and the impacts of meteorological parameters using high temporal resolution data: an application of Environmental Internet of Things in China. Int. J. Sust. Dev. World 20 (3), 238–247.

Enke, W., Spekat, A., 1997. Downscaling climate model outputs into local and regional weather elements by classification and regression. Clim. Res. 8, 195–207.

Fan, J., Rosenfeld, D., Yang, Y., Zhao, C., Leung, L.R., Li, Z., 2015. Substantial contribution of anthropogenic air pollution to catastrophic floods in Southwest China. Geophys. Res. Lett. 43 (6), 2873–2879.

Feng, J., Hu, J., Xu, B., Hu, X., Sun, P., Han, W., Gu, Z., Yu, X., Wu, M., 2015. Characteristics and seasonal variation of organic matter in $PM_{2.5}$ at a regional background site of the Yangtze River Delta region, China. Atmos. Environ. 123, 288–297.

Feng, J., Zhong, M., Xu, B., Du, Y., Wu, M., Wang, H., Chen, C., 2014. Concentrations, seasonal and diurnal variations of black carbon in $PM_{2.5}$ in Shanghai, China. Atmos. Res. 147–148, 1–9.

Ganguly, D., Jayaraman, A., Gadhavi, H., Rajesh, T.A., 2005. Features in wavelength dependence of aerosol absorption observed over central India. Geophys. Res. Lett. 32, L13821. https://doi.org/10.1029/2005GL023023.

Guo, Q., Hu, M., Guo, S., Wu, Z., Hu, W., Peng, J., Hu, W., Wu, Y., Yuan, B., Zhang, Q., Song, Y., 2015. The identification of source regions of black carbon at a receptor site off the eastern coast of China. Atmos. Environ. 100, 78–84.

Gustafsson, O., Ramanathan, V., 2016. Convergence on climate warming by black carbon aerosols. P. Natl. Acad. Sci. USA 113 (16), 4243–4245.

Hansen, A.D.A., Rosen, H., Novakov, T., 1984. The aethalometer: an instrument for the real-time measurements of optical absorption by aerosol particles. Sci. Total Environ. 36, 191–196.

Healy, R.M., Sciare, J., Poulain, L., Kamili, K., Merkel, M., Muller, T., Wiedensohler, A., Eckhardt, S., Stohl, A., Sarda-Estève, R., McGillicuddy, E., O'Connor, I.P., Sodeau, J.R., Wenger, J.C., 2012. Sources and mixing state of size-resolved elemental carbon particles in a European megacity: Paris. Atmos. Chem. Phys. 12, 1681–1700.

Hopke, P.K., Barrie, L.A., Li, S.M., Cheng, M.D., Li, C., Xie, Y., 1995. Possible sources and preferred pathways for biogenic and non-sea salt sulfur for the high Arctic. J. Geophys. Res.-Atmos. 100 (D8), 16595–16603.

Hsu, Y.K., Holsen, T.M., Hopke, P.K., 2003. Comparison of hybrid receptor models to locate PCB sources in Chicago. Atmos. Environ. 37, 545–562.

Huang, X., Ding, A.J., Liu, L., Liu, Q., Ding, K., Niu, X., Nie, W., Xu, Z., Chi, X., Wang, M., Sun, J., Guo, W., Fu, C., 2016. Effects of aerosol-radiation interaction on precipitation during biomass-burning season in East China. Atmos. Chem. Phys. 16, 10063–10082.

Husain, L., Dutkiewicz, V.A., Khan, A.J., Ghauri, B.M., 2007. Characterization of carbonaceous aerosols in urban air. Atmos. Environ. 41, 6872–6883.

Janssen, N.A., Hoek, G., Simic-Lawson, M., Fischer, P., van Bree, L., ten Brink, H., Keuken, M., Atkinson, R.W., Anderson, H.R., Brunekreef, B., Cassee, F.R., 2011. Black carbon as an additional indicator of the adverse health effects of airborne particulate compared with PM_{10} and $PM_{2.5}$. Environ. Health Perspect. 119 (12), 1691–1699.

Joshi, H., Naja, M., Singh, K.P., Kumar, R., Bhardwaj, P., Babu, S.S., Satheesh, S.K., Moorthy, K.K., Chandola, H.C., 2016. Investigations of aerosol black carbon from a semi-urban site in the Indo-Gangetic Plain region. Atmos. Environ. 125, 346–359.

Kalogridis, A.C., Vratolis, S., Liakakou, E., Gerasopoulos, E., Mihalopoulos, N., Eleftheriadis, K., 2018. Assessment of wood burning versus fossil fuel contribution to wintertime black carbon and carbon monoxide concentrations in Athens, Greece. Atmos. Chem. Phys. 18, 10219–10236.

Lee, G., Kim, P., Han, Y., Holsen, T., Lee, S., 2014. Tracing sources of total gaseous mercury to Yongheung Island off the coast of Korea. Atmosphere 5, 273–291.

Li, M., Zhang, Q., Kurokawa, J., Woo, J.H., He, K., Lu, Z., Ohara, T., Song, Y., Streets, D.G., Carmichael, G.R., Cheng, Y.F., Hong, C.P., Huo, H., Jiang, X., Kang, S., Liu, F., Su, H., Zheng, B., 2017. MIX: a mosaic Asian anthropogenic emission inventory under the international collaboration framework of the MICS-Asia and HTAP. Atmos. Chem. Phys. 17, 935–963.

Liao, Z., Gao, M., Sun, J., Fan, S., 2017. The impact of synoptic circulation on air quality and pollution-related human health in the Yangtze River Delta region. Sci. Total Environ. 607–608, 838–846.

Liu, S., Xing, J., Zhao, B., Wang, J., Wang, S., Zhang, X., Ding, A., 2019. Understanding of aerosol-climate interactions in China: aerosol impacts on solar radiation, temperature, cloud, and precipitation and its changes under future climate and emission scenarios. Curr. Pollution Rep. 5, 36–51.

Liu, Y., Yan, C., Zheng, M., 2018. Source apportionment of black carbon during winter in Beijing. Sci. Total Environ. 618, 531–541.

Lupu, A., Maenhaut, W., 2002. Application and comparison of two statistical

trajectory techniques for identification of source regions of atmospheric aerosol species. Atmos. Environ. 36 (36–37), 5607–5608.
Miao, Y., Li, J., Miao, S., Che, H., Wang, Y., Zhang, X., Zhu, R., Liu, S., 2019. Interaction between planetary boundary layer and $PM_{2.5}$ pollution in megacities in China: a review. Curr. Pollution Rep. https://doi.org/10.1007/s40726-019-00124-5.
Mousavi, A., Sowlat, M.H., Lovett, C., Rauber, M., Szidat, S., Boffi, R., Borgini, A., Marco, C.D., Ruprecht, A.A., Sioutas, C., 2019. Source apportionment of black carbon (BC) from fossil fuel and biomass burning in metropolitan Milan, Italy. Atmos. Environ. Times 203, 252–261.
Nichols, J.L., Owens, E.O., Dutton, S.J., Luben, T.J., 2013. Systematic review of the effects of black carbon on cardiovascular disease among individuals with pre-existing disease. Int. J. Public Health 58 (5), 707–724.
Niu, S., Zhang, Q., 2010. Scattering and absorption coefficients of aerosols in a semi-arid area in China: diurnal cycle, seasonal variability and dust events. Asia-Pac. J. Atmos. Sci. 46 (1), 65–71.
Peng, J., Hu, M., Guo, S., Du, Z., Zheng, J., Shang, D., Zamora, M.L., Zeng, L., Shao, M., Wu, Y.S., Zheng, J., Wang, Y., Glen, C.R., Collins, D.R., Molina, M.J., Zhang, R., 2016. Markedly enhanced absorption and direct radiative forcing of black carbon under polluted urban environments. P. Natl. Acad. Sci. USA 113 (16), 4266–4271.
Philipp, A., Bartholy, J., Beck, C., Erpicum, M., Esteban, P., Fettweis, X., Huth, R., James, P., Jourdain, S., Kreienkamp, F., Krennert, T., Lykoudis, S., Michalides, S.C., Pianko-Kluczynska, K., Post, P., Alvarez, D.R., Schiemann, R., Spekat, A., Tymvios, F.S., 2010. Cost733cat–A database of weather and circulation type classifications. Phys. Chem. Earth 35 (9–12), 360–373.
Philipp, A., Beck, C., Esteban, P., Kreienkamp, F., Krennert, T., Lykoudis, S., Pianko-Kluczynska, K., Post, P., 2014. cost733class-1.2 User Guide.
Polissar, A.V., Hopke, P.K., Paatero, P., Kaufmann, Y.J., Hall, D.K., Bodhaine, B.A., Dutton, E.G., Harris, J.M., 1999. The aerosol at Barrow, Alaska: long-term trends and source locations. Atmos. Environ. 33, 2441–2458.
Pope, R.J., Savage, N.H., Chipperfield, M.P., Ordonez, C., Neal, L.S., 2015. The influence of synoptic weather regimes on UK air quality: regional model studies of tropospheric column NO_2. Atmos. Chem. Phys. 15, 11201–11215.
Qiu, Y., Wu, X., Zhang, Y., Xu, L., Hong, Y., Chen, J., Chen, X., Deng, J., 2019. Aerosol light absorption in a coastal city in Southeast China: temporal variations and implications for brown carbon. J. Environ. Sci. 80, 257–266.
Ramanathan, V., Carmichael, G., 2008. Global and regional climate changes due to black carbon. Nat. Geosci. 1, 221–227.
Ran, L., Deng, Z.Z., Wang, P.C., Xia, X.A., 2016. Black carbon and wavelength-dependent aerosol absorption in the North China Plain based on two-year aethalometer measurements. Atmos. Environ. 142, 132–144.
Reche, C., Querol, X., Alastuey, A., Viana, M., Pey, J., Moreno, T., Rodriguez, S., Gonzalez, Y., Femandez-Camacho, R., de la Rosa, J., Dall'Osto, M., Prevot, A.S.H., Hueglin, C., Harrison, R.M., Quincey, P., 2011. New considerations for PM, black carbon and particle number concentration for air quality monitoring across different European cities. Atmos. Chem. Phys. 11, 6207–6227.
Reddy, B.S.K., Kumar, K.R., Balakrishnaiah, G., Gopal, K.R., Reddy, R.R., Reddy, L.S.S., Ahammed, Y.N., Narasimhulu, K., Moorthy, K.K., Babu, S.S., 2012. Potential source regions contributing to seasonal variations of black carbon aerosols over Anantapur in Southeast India. Aerosol Air Qual. Res. 12, 344–358.
Sandradewi, J., Prevot, A.S.H., Szidat, S., Perron, N., Alfarra, M.R., Lanz, V.A., Weingartner, E., Baltensperger, U., 2008. Using aerosol light absorption measurements for the quantitative determination of wood burning and traffic emission contributions to particulate matter. Environ. Sci. Technol. 42 (9), 3316–3323.
Shen, L., Li, L., Lv, S., Zhang, X., Liu, J., An, J., Zhang, G., Wu, B., Wang, F., 2015. Characteristics of black carbon aerosol in Jiaxing, China during autumn 2013. Particuology 20, 10–15.
Simpson, M., Raman, S., Lundquist, J.K., Leach, M., 2007. A study of the variation of urban mixed layer heights. Atmos. Environ. 41, 6923–6930.
Srivastava, A.K., Singh, S., Pant, P., Dumka, U.C., 2012. Characteristics of black carbon over Delhi and Manora Peak – a comparative study. Atmos. Sci. Lett. 13, 223–230.
Stein, A.F., Draxler, R.R., Rolph, G.D., Stunder, B.J.B., Cohen, M.D., Ngan, F., 2015. NOAA's HYSPLIT atmospheric transport and dispersion modeling system. Bull. Am. Meteorol. Soc. 96, 2059–2077.
Sun, J., Huang, L., Liao, H., Li, J., Hu, J., 2017. Impacts of regional transport on particulate matter pollution in China: a review of methods and results. Curr. Pollution Rep. 3, 182–191.
Tiwari, S., Srivastava, A.K., Bisht, D.S., Parmita, P., Srivastava, M.L., Attri, S.D., 2013. Diurnal and seasonal variations of black carbon and $PM_{2.5}$ over New Delhi, India: influence of meteorology. Atmos. Res. 125–126, 50–62.
Vaishya, A., Singh, P., Rastogi, S., Babu, S.S., 2017. Aerosol black carbon quantification in the central Indo-Gangetic Plain: seasonal heterogeneity and source apportionment. Atmos. Res. 185, 13–21.
Virkkula, A., Mäkelä, T., Hillamo, R., Yli-Tuomi, T., Hirsikko, A., Hämeri, K., Koponen, I.K., 2007. A simple procedure for correcting loading effects of Aethalometer data. J. Air Waste Manage. 57 (10), 1214–1222.
Wang, Q., Huang, R.J., Zhao, Z., Zhang, N., Wang, C., Ni, H., Tie, X., Han, Y., Zhuang, M., Wang, M., Zhang, J., Zhang, X., Dusek, U., Cao, J., 2016. Size distribution and mixing state of refractory black carbon aerosol from a coastal city in South China. Atmos. Res. 181, 163–171.
Wang, R., Tao, S., Wang, W., Liu, J., Shen, H., Shen, G., Wang, B., Liu, X., Li, W., Huang, Y., Zhang, Y., Lu, Y., Chen, H., Chen, Y., Wang, C., Zhu, D., Wang, X., Li, B., Liu, W., Ma, J., 2012. Black carbon emissions in China from 1949 to 2050. Environ. Sci. Technol. 46, 7595–7603.
Wang, Q., Huang, R.J., Cao, J.J., Tie, X.X., Ni, H.Y., Zhou, Y.Q., Han, Y.M., Hu, T.F., Zhu, C.S., Feng, T., Li, N., Li, J.D., 2015. Black carbon aerosol in winter northeastern Qinghai-Tibetan Plateau, China: the source, mixing state and optical property. Atmos. Chem. Phys. 15, 13059–13069.
Watson, J.G., Chow, J.C., 2002. Comparison and evaluation of in situ and filter carbon measurements at the Fresno Supersite. J. Geophys. Res.-Atmos. 107, 8341. https://doi.org/10.1029/2001jd000573.
Weingartner, E., Saathoff, H., Schnaiter, M., Streit, N., Bitnar, B., Baltensperger, U., 2003. Absorption of light by soot particles: determination of the absorption coefficient by means of Aethalometers. J. Aerosol Sci. 34, 1445–1463.
Wu, D., Wu, C., Liao, B., Chen, H., Wu, M., Li, F., Tan, H., Deng, T., Li, H., Jiang, D., Yu, J.Z., 2013. Black carbon over the South China Sea and in various continental locations in South China. Atmos. Chem. Phys. 13, 12257–12270.
Yan, J., Chen, L., Lin, Q., Zhao, S., Zhang, M., 2016. Effect of typhoon on atmospheric aerosol particle pollutants accumulation over Xiamen, China. Chemosphere 159, 244–255.
Yan, P., Tang, J., Huang, J., Mao, J.T., Zhou, X.J., Liu, Q., Wang, Z.F., Zhou, H.G., 2008. The measurement of aerosol optical properties at a rural site in Northern China. Atmos. Chem. Phys. 8, 2229–2242.
Zha, S., Cheng, T., Tao, J., Zhang, R., Chen, J., Zhang, Y., Leng, C., Zhang, D., Du, J., 2014. Characteristics and relevant remote sources of black carbon aerosol in Shanghai. Atmos. Res. 135–136, 159–171.
Zhang, J.P., Zhu, T., Zhang, Q.H., Li, C.C., Shu, H.L., Ying, Y., Dai, Z.P., Wang, X., Liu, X.Y., Liang, A.M., Shen, H.X., Yi, B.Q., 2012. The impact of circulation patterns on regional transport pathways and air quality over Beijing and its surroundings. Atmos. Chem. Phys. 12, 5031–5053.
Zhang, Y., Mao, H., Ding, A., Zhou, D., Fu, C., 2013. Impact of synoptic weather patterns on spatio–temporal variation in surface O_3 levels in Hong Kong during 1999–2011. Atmos. Chem. Phys. 73, 41–50.
Zhang, Y., Ding, A., Mao, H., Nie, W., Zhou, D., Liu, L., Huang, X., Fu, C., 2016. Impact of synoptic weather patterns and inter-decadal climate variability on air quality in the North China Plain during 1980–2013. Atmos. Environ. 124, 119–128.
Zhang, Y., Zhang, H., Deng, J., Du, W., Hong, Y., Xu, L., Qiu, Y., Hong, Z., Wu, X., Ma, Q., Yao, J., 2017. Source regions and transport pathways of $PM_{2.5}$ at a regional background site in East China. Atmos. Environ. 167, 202–211.
Zheng, Q.P., Wang, H., Lin, C.C., Chen, X.Q., Liu, H.N., 2013. Characteristics of atmospheric pollutants and its relationships with synoptic situations over the metropolis in the western coast of Taiwan Strait. Acta Sci. Circumstantiae 33 (2), 356–363.
Zheng, X.Y., Fu, Y.F., Yang, Y.J., Liu, G.S., 2015. Impact of atmospheric circulations on aerosol distributions in autumn over eastern China: observational evidence. Atmos. Chem. Phys. 15, 15115–12138.
Zhou, X.H., Cao, J., Wang, T., Wu, W.S., Wang, W.X., 2009. Measurement of black carbon aerosols near two Chinese megacities and the implications for improving emission inventories. Atmos. Environ. 43, 3918–3924.
Zhu, C.S., Cao, J.J., Xu, B.Q., Huang, R.J., Wang, P., Ho, K.F., Shen, Z.X., Liu, S.X., Han, Y.M., Tie, X.X., Zhao, Z., 2016. Black carbon aerosols at Mt. Muztagh Ata, a high-altitude location in the western Tibetan plateau. Aerosol Air Qual. Res. 16, 752–763.
Zhuang, B.L., Liu, L., Shen, F.H., Wang, T.J., Han, Y., 2010. Semi-direct radiative forcing of internal mixed black carbon cloud droplet and its regional climatic effect over China. J. Geophys. Res. 115, D00K19. https://doi.org/10.1029/2009JD013165.
Zhuang, B.L., Wang, T.J., Liu, J., Li, S., Xie, M., Yang, X.Q., Fu, C.B., Sun, J.Y., Yin, C.Q., Liao, J.B., Zhang, Y., 2014. Continuous measurement of black carbon aerosol in urban Nanjing of Yangtze River Delta, China. Atmos. Environ. 89, 415–424.